Hindawi
Geofluids
Volume 2023, Article ID 8554862, 15 pages
https://doi.org/10.1155/2023/8554862

Research Article

Mechanical Properties of In Situ Loess under Different Combined Water State Macroscopic and Mesoscopic Studies

Yueyue Wang, Xuesong Mao, Qian Wu, and Jianxun Zhang

School of Highway, Chang'an University, Xi'an, Shaanxi 710064, China

Correspondence should be addressed to Qian Wu; wuqian@chd.edu.cn

Received 19 August 2022; Revised 5 October 2022; Accepted 8 October 2022; Published 18 February 2023

Academic Editor: Zhengzheng Xie

To study the mechanisms of strong and weak combined water on the mechanical properties of in situ loess deformation and strength, triaxial compression tests with different combined water contents were carried out to in situ loess in a region of Shaanxi Province, China. The influence on the mechanical properties and structural variation of in situ loess was discussed from the perspective of combined water. The endogenous factors of deformation and strength properties of in situ loess in triaxial tests were investigated from a fine-scale perspective by combining numerical simulations of discrete elements. The results show that the failure specimen under the condition of strong combined water has an obvious shear band and shows brittle failure. The failure mode of soil samples under weak combined water is characterized by no obvious cracks and bulging, which is plastic failure. The water content at the boundary of strong and weak combined water is the boundary to distinguish weak and strong strain hardening. With the increase of combined water, the ultimate strength, the structural strength, and structural parameters decrease, and the initial structural parameters decrease nonlinearly, resulting in the decrease of soil structure and deformation resistance. Weak combined water is the main factor affecting soil structure. The particle flow numerical simulation explains the whole process of triaxial test of in situ loess from macro to meso and explains from the meso perspective that the structural strength change of intact loess under different combined water contents is mainly caused by the change of contact force and pore between particles.

1. Introduction

The water within the double electric layer consisting of the negative charge on the surface of the clay particles and the surrounding water molecule dipoles and cation clouds is called combined water, and the water outside the double electron layer is called free water [1]. The arrangement of combined water is much tighter than that of water molecules in general liquid water, so it has a certain shear strength, and decreases with the increase of spacing on the surface of soil particles. The combined water closest to the surface of the soil grain, called "strong combined water," which has great shear strength and viscosity and does not move when the soil, is pressed. The combined water slightly farther from the surface of soil particles is called "weak combined water," and its existence makes the soil plastic. The clay minerals in loess are very easy to interact with water and form adsorbed combined water on the surface of loess particles, which affects the physical parameters and related mechanical properties of loess [2–4].

Since the 1990s, scholars at home and abroad have conducted relevant research on the definition of combined water, water film thickness, change law, and its influence on the physical and mechanical properties of loess [5, 6]. Liu et al., Li et al., and Wang et al. [7–9] classified the types and boundaries of combined water on the loess surface by isothermal adsorption method and thermogravimetric analysis. It is found that the increase of weak combined water content in loess would lead to the increase of water content, and the mineral composition had an important influence on the content of adsorbed combined water. These results promote the in-depth research on the properties of combined

water itself and lay a solid foundation for revealing the mechanism of the influence of combined water on the physical and mechanical properties of soil.

Some scholars have explored the mechanism of the influence of combined water on the physical and mechanical properties of soil and have achieved corresponding research results. He et al. [10] carried out a study on the developmental characteristics of bound water and the shear strength of remodeled loess based on the NMR technique and analyzed the relationship between the bound water content and the shear strength of the soil. Li et al. [11] carried out a series of indoor tests for Shanghai silty clay and quantitatively analyzed the phased variation of combined water during consolidation creep. Xu et al. [12] derived the shear strength of clay combined water as a function of the distance from the combined water to the particle based on the clay bilayer theory and obtained the law that the combined water will move when the water pressure exceeds the "starting shear" of the combined water. Yang [13] obtained the influence mechanism of combined water on the viscosity coefficient of clay through consolidation test. Testamanti and Rezaee [14] conducted a $T2$ test using NMR to investigate the relationship between combined water and pore structure in clays. Wu et al. [15] used soft soil to carry out isothermal adsorption test and consolidation creep test of remolded soil under different combined water content. The influence mechanism of the combined water type on the creep properties of remodeled soils was investigated. Several scholars have demonstrated that the variation of water content has a significant effect on both the angle of internal friction and cohesion of unsaturated loess [16, 17], while the endogenous factor is the effect of the thickness of the combined water film. All of the above studies have only investigated the mechanism of the influence of specific combined water types on the physical and mechanical properties of geotechnical bodies, but there are few comparative analyses. Therefore, in this paper, the deformation characteristics and mechanical properties of in situ loess under different combined water conditions are analyzed and defined in detail.

The special skeletal structure of loess means that there is a certain intrinsic pattern between structural parameters and physical indicators of loess [18, 19], but the connection between combined water and structural parameters is very rarely explored at present. In addition, there are few tests to study the physical and mechanical properties of loess under the influence of combined water by discrete element numerical software [20, 21], mainly focusing on the fine-scale study of water content on the strength properties of loess and the mechanical tests of sandy soil types.

The variation in the type and content of combined water has an important effect on the mechanical properties of in situ loess. In this paper, the in situ loess was used as the research object. First, the combined water in the test soil samples was defined, and then triaxial compression tests were conducted from the perspective of different combined water contents to explore the mechanism on the mechanical properties of in situ loess. Considering that the macroscopic deformation of the soil is caused by the accumulation of fine structural damage, a disadvantage is that only the changes in shape and mechanical indices can be monitored based on macroscopic tests. Therefore, the internal causes of deformation and strength changes of in situ loess in macroscopic triaxial tests were investigated using discrete element numerical software. In this paper, the effects of combined water on the mechanical properties and deformation characteristics of in situ loess are systematically studied from two perspectives: macroscopic and fine.

2. Materials and Methods

2.1. Materials. The test soil samples were taken from a region in Shaanxi, China, and belong to type Q_2 loess. The soil sample was taken from a depth of 16 m below ground, and the gradation curve is shown in Figure 1. The inhomogeneity coefficient of the in situ loess at this site is greater than 5, and the curvature coefficient is between 1 and 3, indicating that it is a well-graded soil. The content of powder particles (0.005~0.075 mm) is more than 68%, and the loess in this area belongs to powdered clay. After adding the dispersant, the content of powder particles increased, indicating that there is a certain amount of "false powder particles" in the loess.

The clay minerals in the soil samples measured by X-ray test mainly contain illite, chlorite, eumonite, and kaolinite (Figure 2), and the clay mineral content accounts for 16.8% of the total minerals. The strong hydrophilic nature of clay minerals causes the loess to sink when wet with water. The soil sample was tested according to the (Highway Geotechnical Test Procedure) (JTG 3430-2020), and its basic physical property indexes are shown in Table 1. The soil sample has the characteristics of larger water content and more developed pore space.

2.2. Specimen Preparation and Test Setup. Li et al. and Zhang et al. [22, 23] used the volumetric flask method to verify that the combined water in clay satisfies the equation: $w_g = 0.885w_p$, where the plastic limit corresponds to the limit of strong and weak combined water association, and the liquid limit corresponds to the limit of weak combined water and saturation. Therefore, the water content corresponding to the strong combined water of the soil sample chosen for this test is 15.85%, when only strong combined water is adsorbed around the clay particles. Weak combined water corresponds to a water content of 15.85% to 30%, and soil samples with a water content greater than 30% are in a saturated state.

In situ soil samples with strong combined water content of 5%, 10%, 13%, and 15% were produced by humidification titration and shade drying methods, respectively. In situ soil columns with predominantly weak combined water (20%, 25%, and 30%) and saturated water content (34%) were prepared. Each soil sample was stored for 72 h to make the moisture uniformly distributed. After that, using a soil cutter, the soil column was cut into a specimen with a diameter of 39.1 mm and a height of 80 mm.

The preparation of the remodeled soil specimen was done by drying the as-built soil at 105°C, crushing it and passing it through a 2 mm sieve, and then adding water

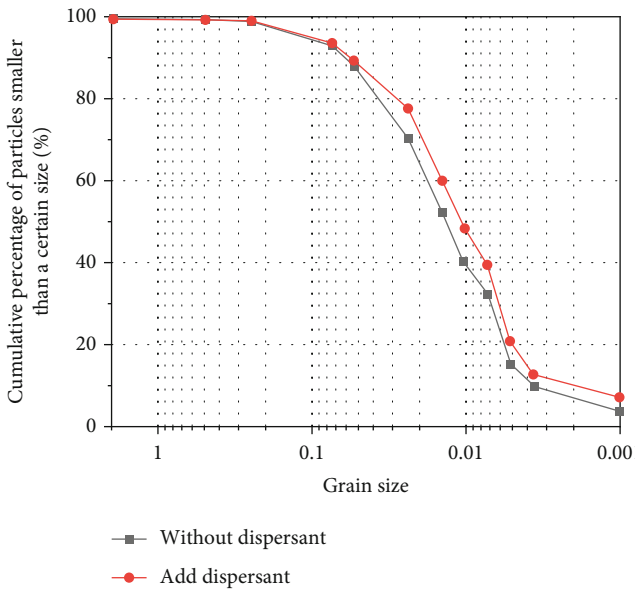

Figure 1: Particle gradation curve.

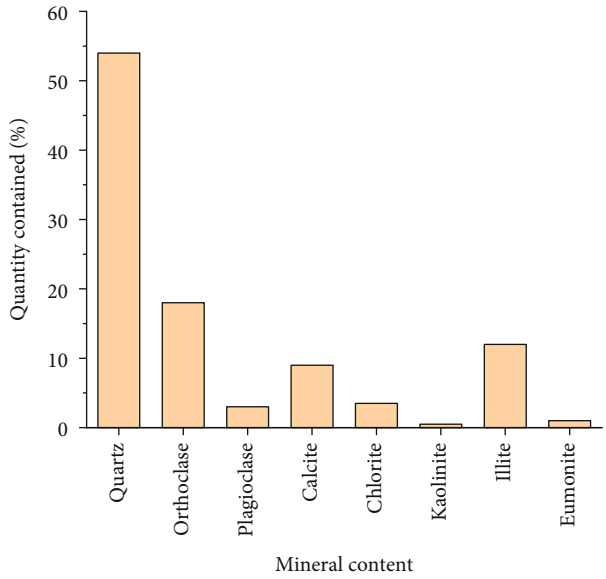

Figure 2: Mineral content statistics.

uniformly according to the moisture content of 34%, and the required amount of water for the specimen (m_w) is shown in equation (1). The soil material was kept sealed for 2 ~ 3 days, and then the desired specimen was made in the sample maker using the method of layered compaction. Then, it is compacted by hydraulic pump and saturated.

$$m_w = \frac{m}{1 + 0.01w_h} \times 0.01(w - w_h), \quad (1)$$

where m is the mass of the soil sample corresponding to the air-dried water content (g), w_h is the air-dried water content (%), and w is the desired water content (%).

The test apparatus is GDS static triaxial instrument made in UK, which consists of pressure system, channel acquisition device, acquisition software system, and sensors. The pressure chamber of this equipment uses gas as the transfer medium of the surrounding pressure, and the surrounding pressure is applied to the deaerated water in the pressure chamber by the gas; then, the water applies the surrounding pressure to the specimen. The detailed test preparation process is shown in Figure 3.

2.3. Test Methods. Triaxial consolidation undrained shear tests were performed on the specimens under each combined water content, and the test protocols are shown in Table 2. The test procedure includes specimen mounting, consolidation, and shear. It is worth noting that the drainage valve was opened during consolidation, setting the surrounding pressure at 150 kPa; the drainage valve was closed during shearing and no drainage was allowed during the process, with a shear rate of 1.5 mm/min; stop the test when the axial strain value was 15%. After the test, all damaged soil samples were reasonably sealed and stored to prevent moisture loss.

3. Analysis of Triaxial Compression Test Results of In Situ Loess

3.1. Deformation and Failure Modes of In Situ Loess. The specimen images of shear failure with different combined water contents under triaxial compression test are shown in Figure 4. The analysis shows that the deformation damage form is influenced by the combined water content. From Figures 4(a)–4(c), it can be seen that the damaged specimens in the strong combined water condition had obvious cracks and shear bands, which were brittle damage. The higher the content of weak combined water in the soil (Figures 4(d)–4(f)), the higher the damage of the soil sample in the form of no obvious cracks and the overall bulging, plastic damage. When the water content reached saturation (Figure 4(g)), the shear-damaged soil sample showed greater shear deformation, which was due to the microstructural characteristics of loess with large pores and weak cementation. This feature results in greater shear deformation as the cementation structure of saturated loess was further damaged by the influence of water immersion.

3.2. Mechanical Properties Analysis of In Situ Loess

3.2.1. Stress-Strain Characteristic. Figure 5 shows the stress-axial strain relationship curves of in situ loess with different combined water contents. The curve was generally strain-hardening, which mainly underwent two stages: the first stage was the straight line segment where elastic deformation occurs, and the second stage was the yield stage. In the second stage, the number of new cracks continued to increase with increasing load, when the strain increased faster than the stress value, thus causing a bend in the curve form in this stage. In the stage of strong combined water ($w \le 15\%$), the stress-strain curve was weakly hardening. In the stage of weak combined water ($15\% < w \le 30\%$), the curve was

Table 1: Basic physical property indicators of in situ loess.

Depth (m)	Density (g·cm-3)	Natural moisture content (%)	Specific gravity of soil particles	Dry density (g·cm-3)	Void ratio	Liquid limit (%)	Plasticity index
16.0	1.87	17.50	2.70	1.59	0.93	29.86	11.61

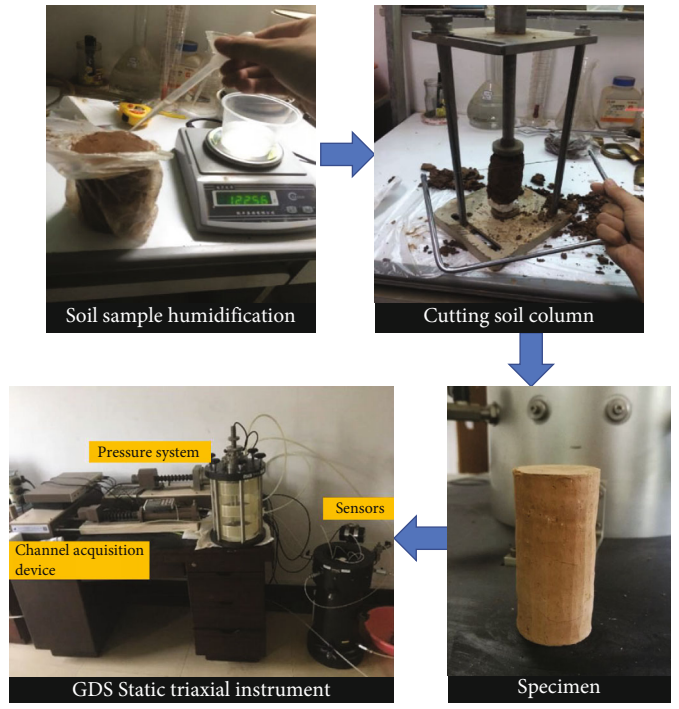

Figure 3: Test preparation process.

Table 2: Triaxial shear test protocol for different combined water conditions.

Surrounding pressure (kPa)	150						
Water content (%)	Strong combined water state			Weak combined water state			Saturated state
	5	10	15	20	25	30	34
Shear rate (mm/min)	1.5						

strongly hardened. Therefore, the water content at the corresponding boundary of combined water can be regarded as the boundary to distinguish weak and strong strain hardening.

The combined water content has an important effect on the strength properties of the in situ loess. The peak of the curve gradually decreased with the increase of the combined water content. This was due to the fact that the thinner the combined water film was, the more viscous the combined water was, and the soil particles wanted to overcome the friction and produce movement was more difficult, which made the stress value of the in situ loess in the strong combined water condition much larger than that in the weak combined water condition. Under the small initial stress, the soil deformation increased with the increase of combined water content, and the yield stress decreased gradually. The remodeled saturated loess was not structural, and the stress value decreased substantially with increasing strain.

3.2.2. Effect of Combined Water on Ultimate Strength. The ultimate strength refers to the ultimate capacity of the soil to resist shear, which can determine whether the soil reaches the shear failure state. If the stress-strain curve has an obvious peak, the peak stress is used as the ultimate strength value; otherwise, the difference in principal stress corresponding to 15% strain value is used as the ultimate strength value.

The ultimate strength decreased with the increase of combined water content (Figure 6). It proved that strong combined water can effectively increase the friction coefficient between particles and improve the shear resistance. Under the condition of weak combined water, the soluble

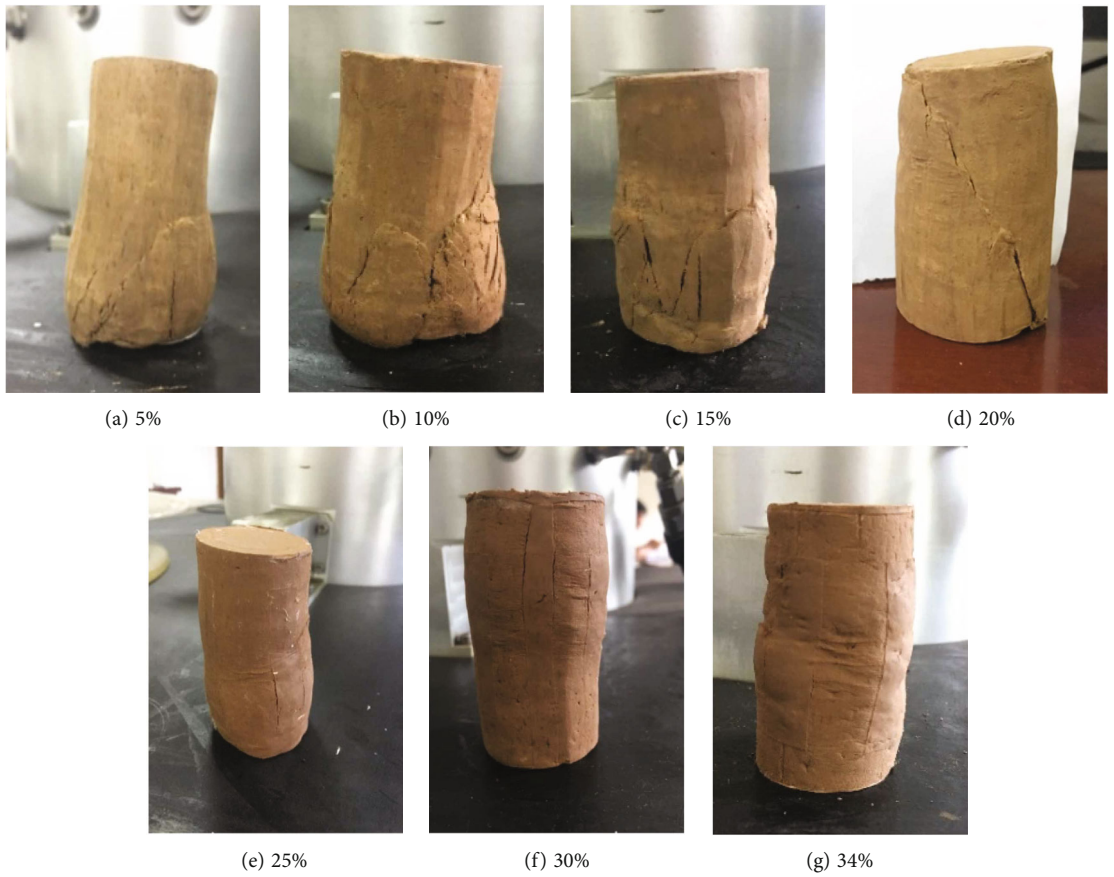

(a) 5% (b) 10% (c) 15% (d) 20%

(e) 25% (f) 30% (g) 34%

Figure 4: Diagram of damaged specimens with different combined water content: (a–c) damaged specimens under strongly combined water condition, (d–f) damaged specimens under weakly combined water condition, and (g) destructive specimens in saturated condition.

matter between soil particles in undisturbed loess was dissolved in water, and the thicker water film also made the cohesion between particles reduce greatly, which made the ultimate strength of this stage reduced rapidly.

3.3. Structural Change Characteristics

3.3.1. Combined Water and Structural Strength Relationship. The pressure corresponding to the turning point of the compression curve is called the structural strength (p_c) [24]. Combined with the previous research results of the group on the compression curve of in situ loess [25], the variation curve of p_c with combined water content was plotted (Figure 7). The analysis shows that the p_c gradually decreased with the increase of the combined water content, and even if the saturated water content (34%) was reached, a smaller structural strength would still exist. As the cohesion and internal friction angle of the in situ loess decrease with the thickening of the combined water film, and in situ loess has a more specific hollow structure and particle linkage strength [26], the deformation of the soil increased under the load. Compared with the in situ loess in the weak combined water condition, the stress required to resist compressive deformation was increased in the strong combined water condition, resulting in greater p_c and soil resistance to deformation. Therefore, the combined water has a greater influence on the structural properties of the in situ loess, among which the weak combined water is the most important.

3.3.2. The Effect of Combined Water on Structural Properties. The structural potential of the soil can be fully released with disturbance, loading, and water immersion. It is only necessary to conduct triaxial tests on undisturbed loess with different combined water contents and remolded saturated loess with the same dry density. Based on the stress-strain curve, the comprehensive structural potential of loess is reflected by the ratio of the principal stress difference $(\sigma_1 - \sigma_3)_y$ to the principal stress difference of remolded saturated loess $(\sigma_1 - \sigma_3)_{rs}$ under the same strain, which is characterized by structural parameter (m_ε). The calculation formula is shown in equation (2). The higher the joint strength of the soil, the greater the strength loss under external forces after loading and water immersion, resulting in the m_ε increased and reflecting the structural change in the in situ loess is more obvious during the triaxial compression test.

$$m_\varepsilon = \frac{(\sigma_1 - \sigma_3)_y}{(\sigma_1 - \sigma_3)_{rs}}. \tag{2}$$

The variation curves of structural parameters of in situ loess are plotted in. The curve trend under different

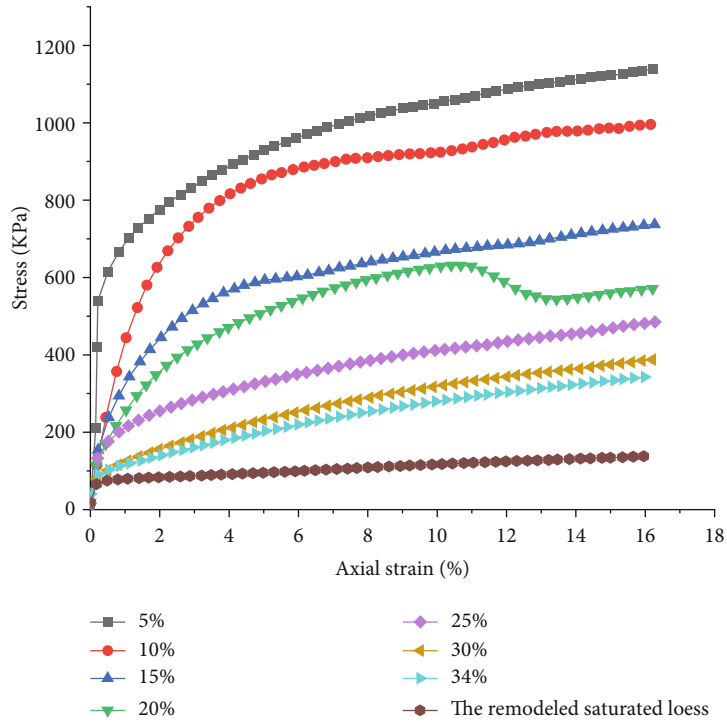

Figure 5: Stress-strain curves of in situ loess under different combined water conditions.

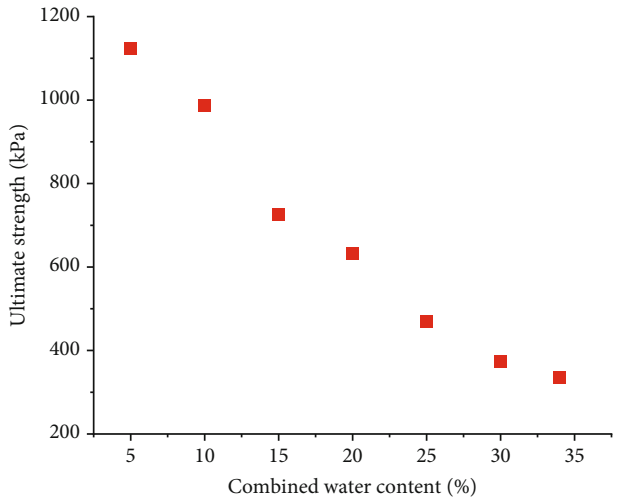

Figure 6: The variation of ultimate strength with combined water content.

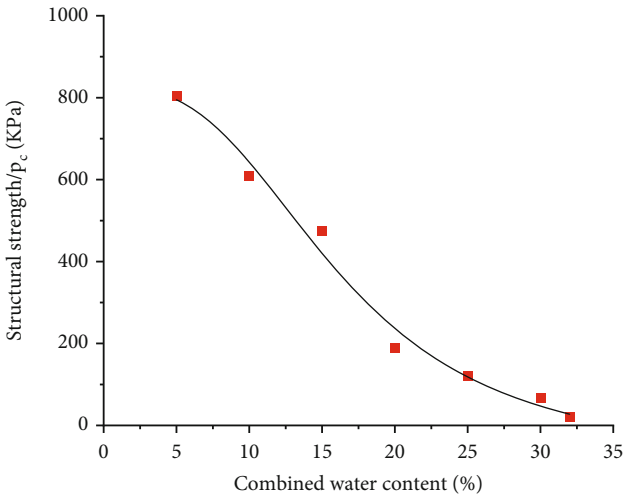

Figure 7: Variation curve of structural strength with combined water content of in situ loess.

combined water conditions was consistent with the stress-strain curves (Figure 8). The peak value of the curve decreased with the increase of combined water content, and the structure gradually weakened. In the stage of strong combined water ($w \leq 15\%$), m_ε increased firstly and then decreased with the increase of axial strain; in the stage of weak combined water ($15\% < w \leq 30\%$) and saturated stage ($w = 34\%$), the curve increased firstly and then gradually flatten.

Combined with Figure 7, the p_c was basically equal to the pressure value corresponding to the peak point of structural parameters under the same moisture content. For example, at $w = 5\%$, the p_c was 800 kPa while the pressure value corresponding to the peak point of m_ε was 830 kPa. This indicated that before the pressure reached p_c, the soil structure was in the compacted stage, in which the thinner the water film thickness was, the less the soil particles undergo misalignment when pressurized, making the m_ε gradually increased (Figure 8). With the pressure greater than p_c, the m_ε in the strong combined water stage gradually decreased, and the in situ loess structure began to break down, showing brittle failure. Under the action of weak combined water

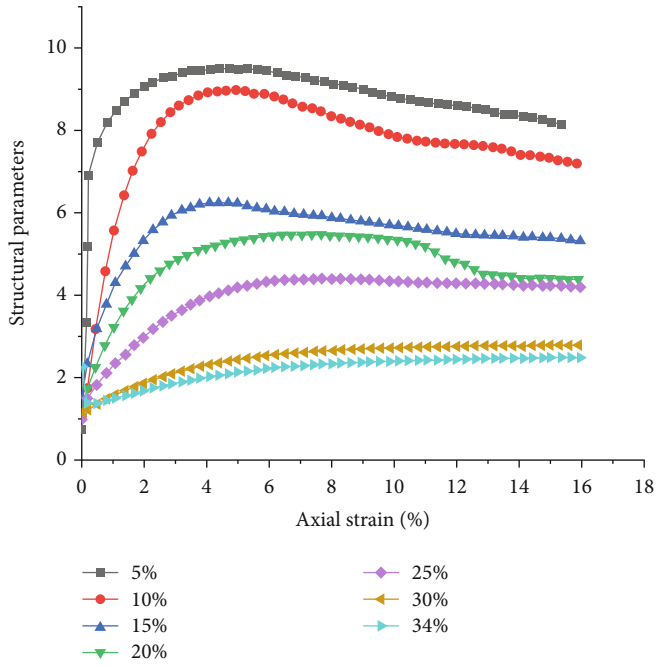

Figure 8: Variation curve of structural parameters with combined water content.

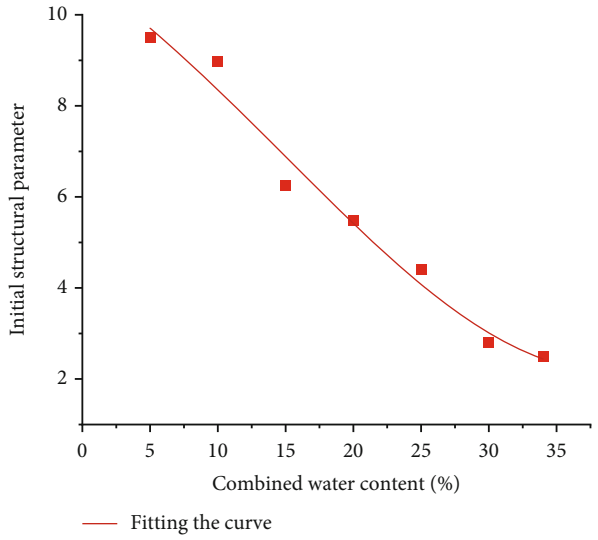

Figure 9: Variation curve of initial structural parameter with combined water content.

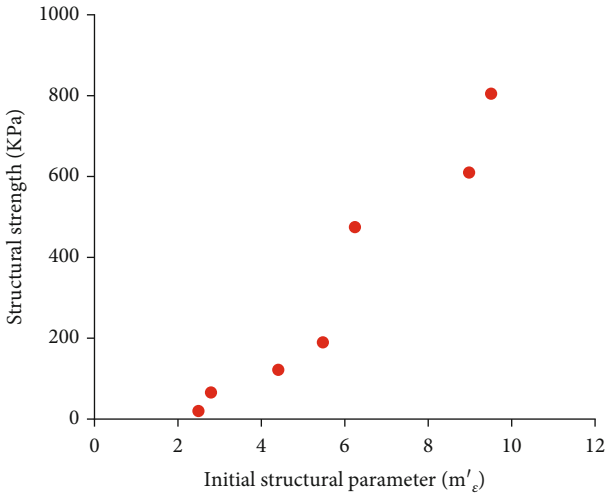

Figure 10: The relationship of p_c with m'_ε.

film, the cohesive force between particles was adjusted with the external force, so that the m_ε of the undisturbed loess increased slightly and showed plastic failure. The weak combined water and free water in the saturated in situ loess were filled with intergranular pores, which greatly weakened the intergranular bonding strength and made the m_ε much smaller than that of the in situ loess with low moisture content. Therefore, the m_ε was strongly influenced by the weak combined water content, and its response mechanism to the combined water content can provide a reasonable explanation for the deformation and damage characteristics of the in situ loess.

The change process of the m_ε is "rising first and then falling" type curve, and the peak value of the m_ε can be used as the parameter of the maximum comprehensive structural potential before the damage of in situ loess, namely, the initial structural parameter (m'_ε) [27]. It reflects the structural properties of the loess in the absence of external disturbance (rainfall, loading, and disturbance). m'_ε decreased nonlinearly and the decrease rate reduced gradually with the increase of combined water content (Figure 9). This shows that the combined water will accelerate the damage of the skeleton structure. Strong combined water made the soil have stronger initial stress structure. In addition, the cementation and connection strength between soil particles was

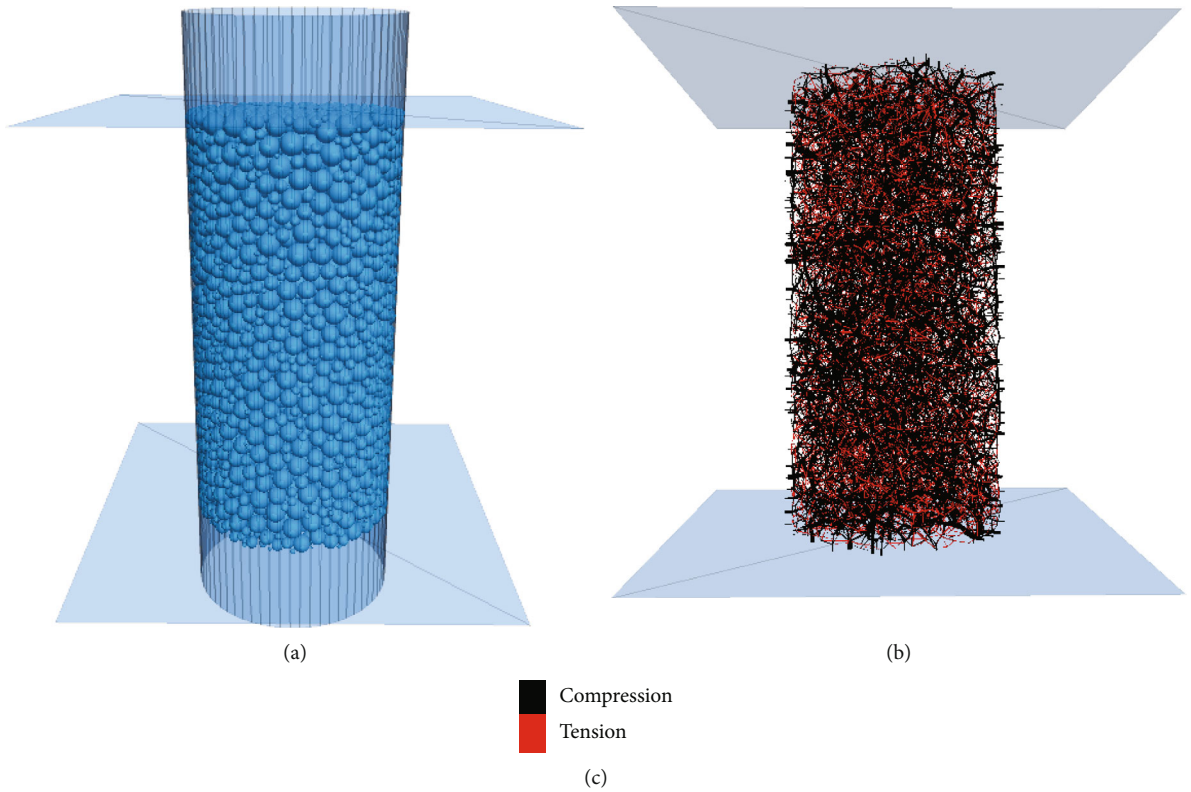

Figure 11: The computational model: (a) generation of the model, (b) contact force chain diagram, and (c) legend.

gradually lost due to the increase of water film thickness, which led to the stability of the structure under stress to be more easily destroyed.

Physical properties such as moisture and structure affect the strength of in situ loess. The different physical properties cause the variability of structural parameters. Figures 7 and 9 were processed to obtain the relationship between the structural strength (p_c) and m'_ε for different combined water conditions (Figure 10). p_c increases nonlinearly with the increase of m'_ε. It shows that m'_ε can reflect the influence of the variation of combined water on the strength parameters of in situ loess.

4. Numerical Analysis of Triaxial Compression Test Based on Discrete Element Method

To further analyze the internal causes of deformation and strength change of undisturbed loess in the macro triaxial test from the microscopic viewpoint, Particle Flow Code in 3D was used to simulate the triaxial compression test of in situ loess under strong and weak combined water conditions.

4.1. Model Establishment and Parameter Determination

4.1.1. Model Establishment. The model dimensions were the same as those of the laboratory test, the diameter of the model was 39.1 mm, and the height was 80 mm. Considering the influence of particle size effect, according to the grain size distribution curve of loess, 8336 particles with a particle size range of 0.1 mm~2 mm were generated. The model carries out the servo mechanism through fish language to load the specimen by moving the wall, and the load generated by moving at each time step is calculated by equation (3). The servo mechanism can simulate the loading of top and bottom walls and simulate the cylindrical wall as the boundary of the enclosing pressure constraint. The intergranular contact is a contact bond model, and when the model is locally deformed or shear bands are generated, the interparticle force chain breaks and reconnects, creating stress concentrations. The computational model is shown in Figure 11.

$$\Delta F^{(w)} = k_n^{(w)} N_c u^{(w)} \Delta t, \tag{3}$$

where N_c is the number of particles in contact with the wall; $k_n^{(w)}$ is the average stiffness; Δt is the time duration per step.

4.1.2. Calibration and Selection of Model Fine Mechanical Parameters. Due to the different parameter systems in macroscopic materials and numerical models, certain computational transformations are required. In this paper, friction coefficient (μ), effective modulus (E^*), stiffness ratio (K^*), tensile strength (T_σ), and shear strength (S_σ) were calibrated separately. On the basis of keeping the remaining basic parameters of the PFC model unchanged, the stress-strain curves were obtained by varying the values of the above parameters, respectively; then, the relationship curves

between the macromechanical parameters and the fine parameters were fitted to determine the fitting equations; finally, the results were dutifully compared with the corresponding indoor test results, to verify the reliability of the calibrated fine parameters.

The friction coefficient (μ) was calibrated using the above method, with μ taking values of 0.4, 0.6, 1.0, 1.2, 1.7, and 2.2, and numerical simulations were performed to obtain the stress-strain curves (Figure 12). The effect of μ on the peak intensity is larger. With the increase of μ, the peak of the curve is increasing, and the slope of the straight line segment of the curve is getting steeper, indicating that the elastic strength is also enhanced. In addition, the curves gradually transitioned from strain-hardening type to strong strain-softening type. The peak intensities corresponding to different parameters were extracted and the relationship curves were fitted (Figure 13), there was a good logarithmic relationship between them, and the functional expression was shown in the following equation.

$$E_\sigma = a + be^{cE_m}, \tag{4}$$

where E_σ is the macromechanical parameter, E_m is the mesoscopic parameter, a, b, and c are the parameters related to the fine structural characteristics of the in situ loess, respectively (Table 3).

Similarly, the calibration results of the other mesoscopic parameters are summarized in Table 3. While T_σ and S_σ act together to affect the stress-strain curve, the limit value for both is 150 kPa after extensive simulations. After simulating the above parameters, the mesoscopic parameters with moisture content of 10% and 25% were obtained, respectively (Table 4).

4.1.3. Test and Monitoring Scheme. Under the condition that the surrounding pressure was 150 kPa and the loading rate of the upper wall was 1.5 mm/min, the models with 10% and 25% of water content were selected for the test, respectively. The suitability of the simulation results to macroscopic tests was analyzed from the perspectives of shear damage surface and stress-strain curves; the endogenous factors of strength variation of in situ loess specimens in macroscopic triaxial tests were investigated from the perspectives of contact force distribution between particles and porosity. This test monitored the porosity distribution state within the model with the help of measuring balls, each of which has a radius of 4 mm and contains contact with each other, and Figure 14 shows the arrangement position of the measuring balls.

4.2. Analysis of Calculation Results

4.2.1. Shear Failure Surface Analysis. Figure 15 shows the simulation results of the model in the strong and weak combined water states, respectively. The legend indicates the magnitude of the particle Euler angle, and the magnitude of its value is proportional to the particle rotation angle. When the combined water content was 10%, the directional movement of particles at the crack generated by the model

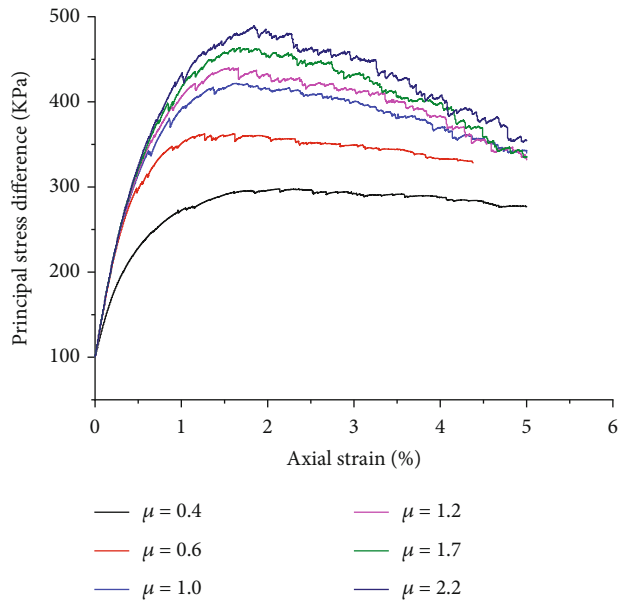

Figure 12: Stress-strain relationship curves at different μ.

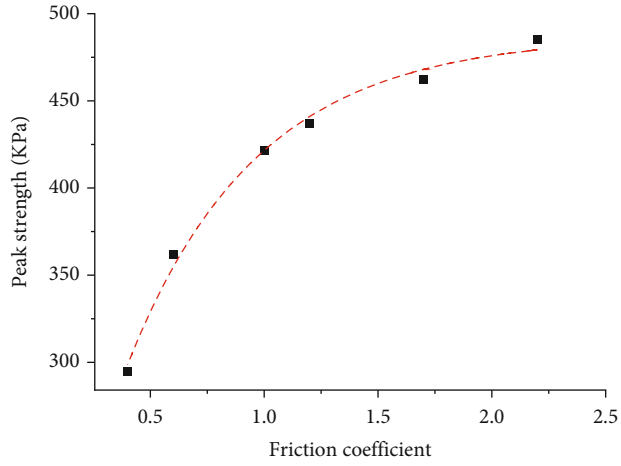

Figure 13: The relationship curve between peak strength and friction coefficient.

was the most obvious and finally developed into a shear band (Figure 15(a)), which is a brittle failure. When the combined water content was 25%, the particles could translate and rotate more easily, because the bonding strength between the particles was reduced to simulate a state with less cohesion. From the particle color in Figure 15(b), it can be seen that the angle of particle rotation at the tiny cracked at the top, bottom, and middle of the specimen was large, and then the macroscopic phenomenon of bulging or shearing was manifested. Comparison with Figures 5(b) and 5(e) shows that the simulation results matched with the actual damage results.

4.2.2. Stress-Strain Curve Analysis. The resultant curves of the numerical simulation of the particle flow could match the macroscopic experimental data better (Figure 16). When the stress-strain curve of the model reached the inflection

Table 3: Relationship between macromechanical parameters and mesoscopic parameters.

E_m	E_σ	a	b	c	R^2
Effective modulus (E^*)	Elastic modulus (E)	52.3624	-49.4837	-0.002	0.9896
Stiffness ratio (K^*)	Elastic modulus (E)	0	176	-0.022	0.938
Friction coefficient (μ)	Peak strength (σ)	487.1914	-381.3007	-1.7592	0.9937

Table 4: Model microscopic parameters.

Water content (%)	Particle density ($kg \cdot m^{-3}$)	Range of particle diameter (mm)	Normal stiffness ($N \cdot m^{-1}$)	Tangential stiffness ($N \cdot m^{-1}$)	Friction factor	Normal bonding strength ($N \cdot m^{-1}$)	Tangential bonding strength ($N \cdot m^{-1}$)
10	2600	0.1 ~2.0	6.0×10^7	6.0×10^7	0.4	1.0×10^1	1.0×10^1
25	2600	0.1 ~2.0	1.0×10^6	1.0×10^6	0.3	1.0×10^0	1.0×10^0
Wall			3.0×10^6	3.0×10^6	0.2		

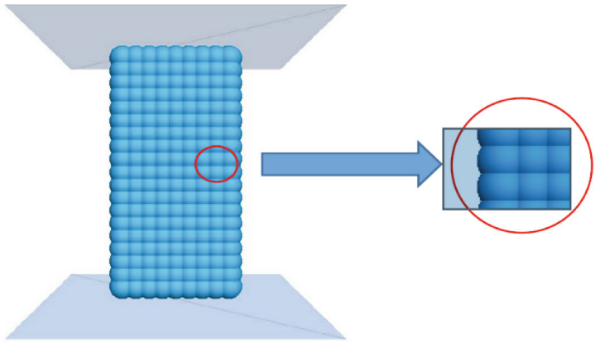

Figure 14: Measuring ball arrangement.

point under the condition of strong combined water, there was a relatively jitter. This was because the bond strength and stiffness between particles were high under this condition. After reaching a certain peak strength, the bond between particles would break and rearrange the contact and form a new bond, resulting in an uneven stress distribution.

4.2.3. Distribution of Contact Forces between Particles. Figure 17 shows the evolution of the contact stresses in the solidification phase, deformation phase, and damage phase for the models with 10% and 25% water content, respectively. Among them, black corresponds to compressive stresses, and red corresponds to tensile stresses, with thicker lines representing higher contact forces.

After starting the shear test, with the downward loading motion of the upper wall, the interparticle compressive stress was along the main stress direction, for the linear elastic change phase. The contact force between the particles in contact with the upper and lower walls was the largest and gradually decreased along the longitudinal direction toward the middle (Figure 17(a)). The tensile stress values had decreased, indicating that the internal microstructure of the soil was being damaged by external forces. The bond strength of the model in the strong combined water state was high, and the contact force showed stress concentration in the region of higher shear strength. The higher compressive stress between particles at the shear zone location indicates that the damage surface will occur along the most unfavorable part under the load (Figure 17(b)).

Similarly, under the action of axial pressure, the contact force of the model dominated by weak combined water gradually increased in the axial direction and decreases in the radial direction (Figure 17(c)). The axial contact force chain of the model in the weak combined water state is thinner than in the strong combined water state; the particles at the upper and lower ends of the model gather and compact, resulting in bulging, and the whole is shear shrinkage damage (Figure 17(d)). It indicates that the interparticle compressive stress acts as the main contact force in the strong combined water condition, and the soil is not prone to shear damage under the lubricating effect. In addition, the adjustment of the particles to the compacting process resulted in an increase in the initial structural properties of the model; as the pressure increased, the interparticle contact linkage is broken, resulting in the destruction of the structural state of the soil and the structural parameters begin to decrease. The movement of the particles indirectly explains the reason for the change of structural parameters of the loess.

4.2.4. Porosity Distribution Analysis. Figure 18 shows the porosity distribution of the models with 10% and 25% water content at different stages, respectively. The porosity of the upper and lower ends of the model was smaller during the shearing process of the test (Figure 18(a)), indicating that the particles in this area were undergoing crowding and compression. When the model reached shear damage (Figure 18(b)), the porosity at the site where the shear zone was located was significantly minimal. This was caused by the fact that a large number of particles at the shear zone site were broken into fine particles by the external force and filled in the pore space, where the large particles were located around.

Under the condition of mainly weak combined water, the porosity of the model after shear failure was clearly distributed with a large middle and small upper and lower ends (Figure 18(d)). Due to the thick water film of weak combined water, the cohesive force between particles was small, which was easy to cause the rotation and translation of the

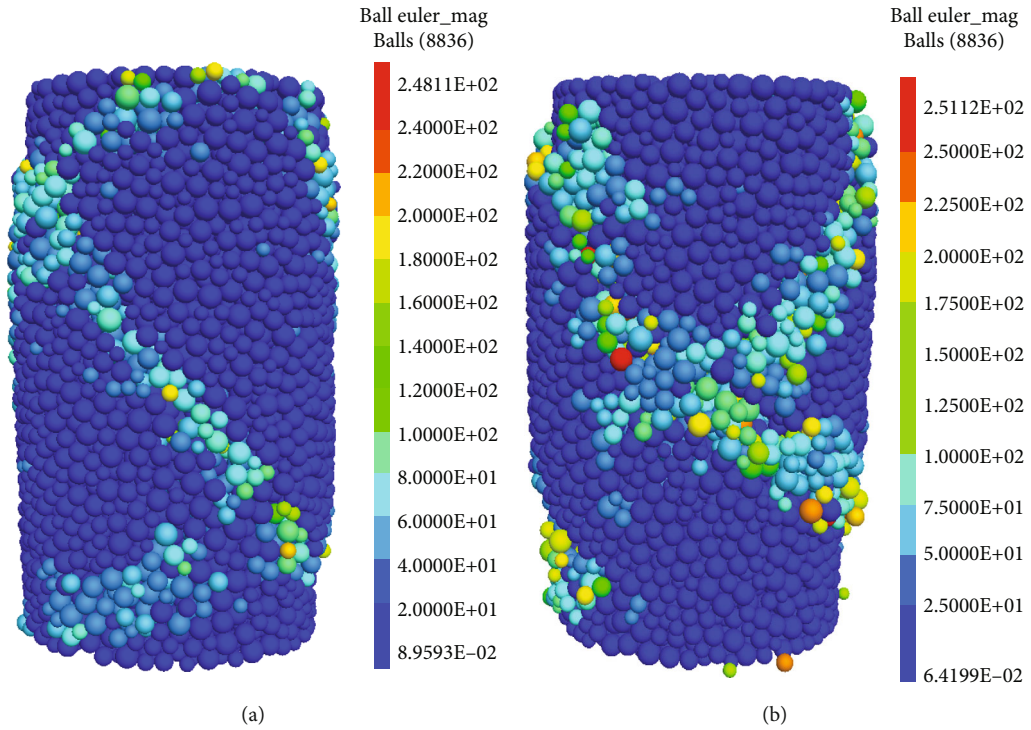

Figure 15: Shear damage surface diagrams with different combined water content: (a) $w = 10\%$ and (b) $w = 25\%$.

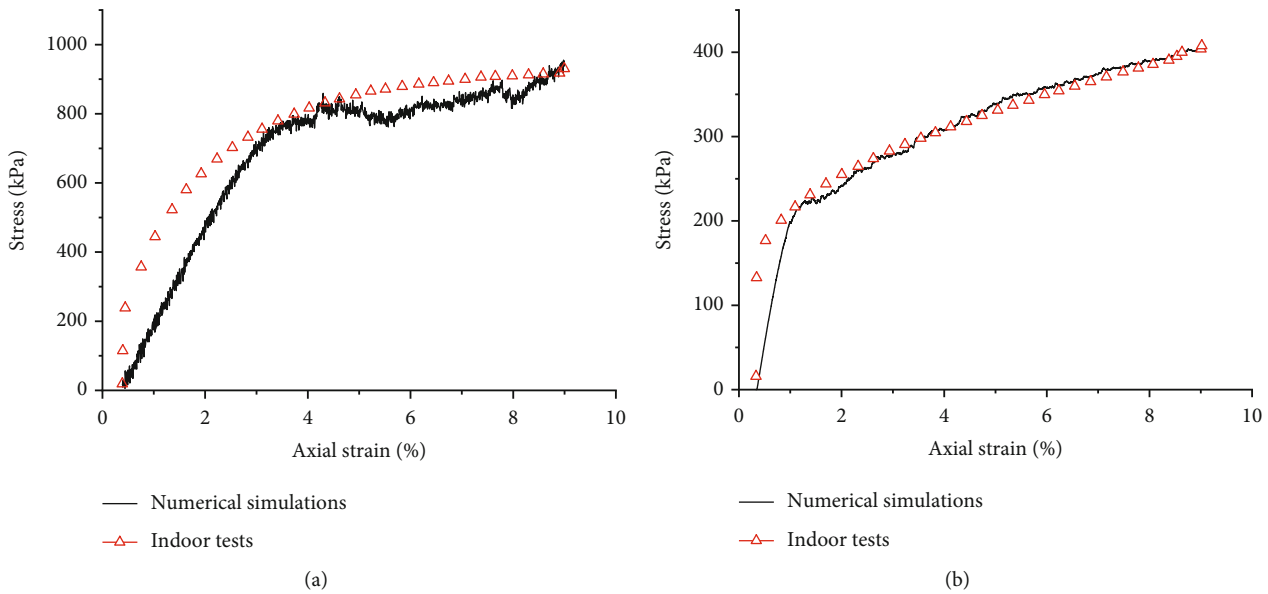

Figure 16: Comparison of stress-strain curves for macro- and meso-tests: (a) $w = 10\%$ and (b) $w = 25\%$.

particles at the upper and lower ends of the larger part of the model under axial external force, and the compaction phenomenon was more prominent, resulting in the decrease of porosity in the region. It was concluded that due to the existence of weak combined water, the porosity is larger than that of the sample with strong combined water under triaxial shear test. These large pores help the particles adjust their angles and positions, releasing deformation energy and thus increasing the ductility of the soil.

5. Discussion

Combined water is an important parameter affecting the mechanical properties and macroscopic performance of in situ loess [28]. In the strong combined water state, the combined water film is thin and viscous, and it is difficult for the soil particles to overcome the friction and move, which makes the shear resistance of the soil body increase. From the PFC simulation, it can be seen that the porosity of the

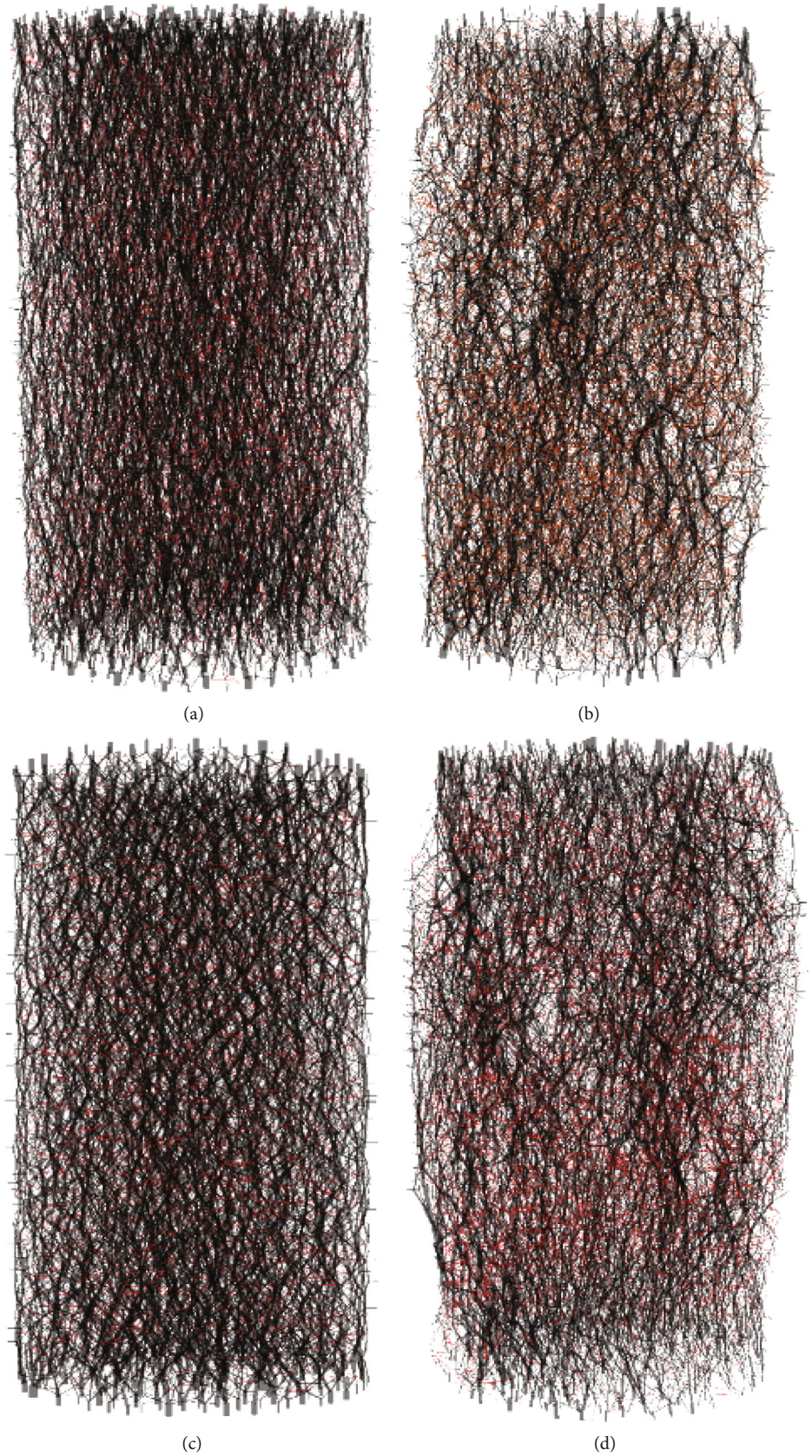

Figure 17: The particle contact force chain at different combined water contents: (a) the deformation phase of $w = 10\%$, (b) the damage phase of $w = 10\%$, (c) the deformation phase of $w = 25\%$, and (d) the damage phase of $w = 25\%$.

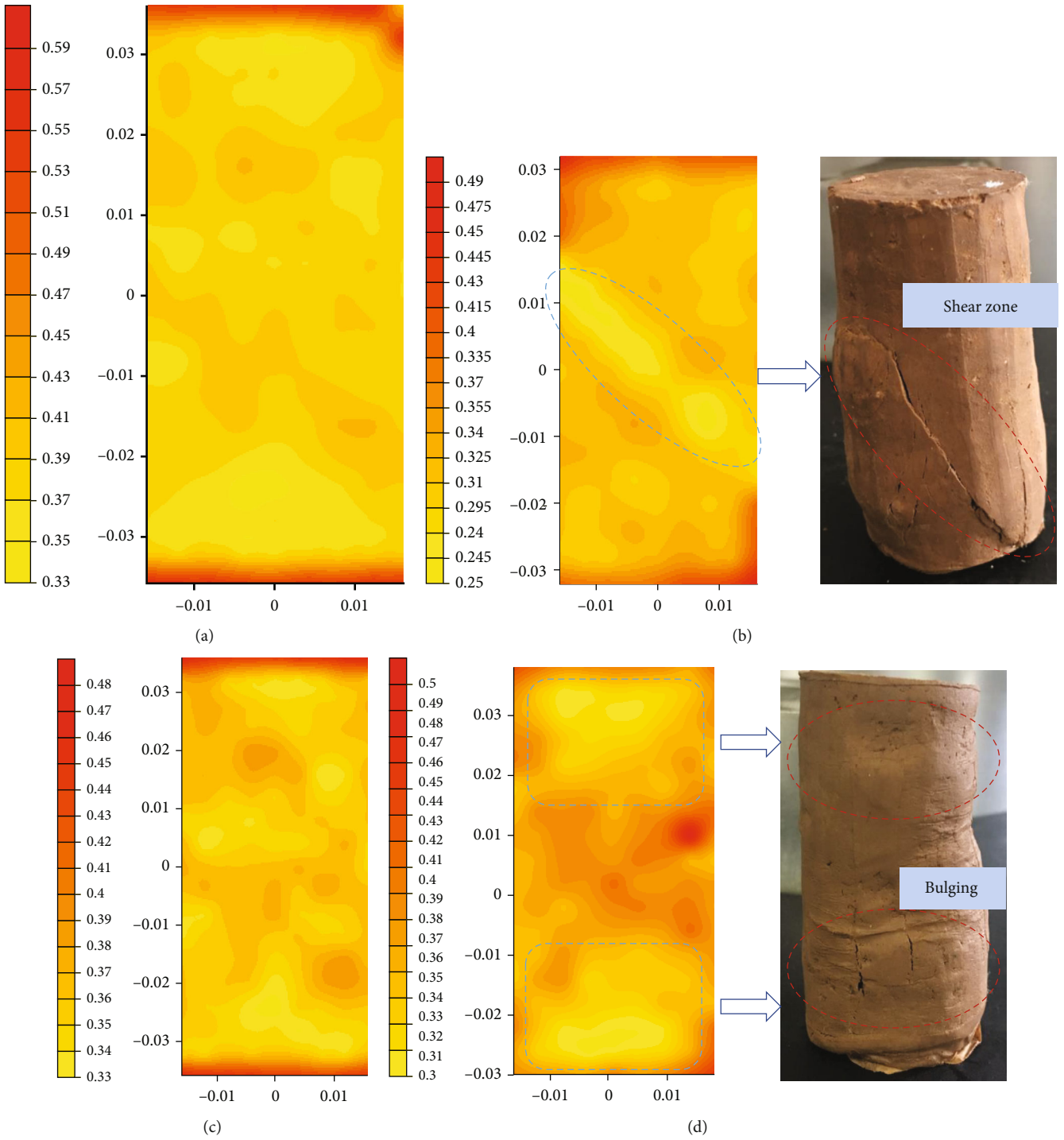

Figure 18: The model porosity distribution maps at different combined water contents: (a) the deformation phase of $w = 10\%$, (b) the damage phase of $w = 10\%$, (c) the deformation phase of $w = 25\%$, and (d) the damage phase of $w = 25\%$.

upper and lower ends of the model is smaller during shear, and the particles in this part are undergoing crowding and compression. The contact force shows stress concentration in the region of higher shear strength, and brittle damage will occur, which indicates that the larger the structural parameter is, the more obvious the structural change of the in-situ loess will be.

In the state of weak combined water, the combined water film thickens, which will gradually dissolve the cementing material between the loess particles; the cohesive force between the particles is lost, and the lower degree of cementation will easily lead to the disintegration of the loess [29]. m_ε is strongly influenced by the weak combined water content, and the variation process of this parameter increasing

and then decreasing indicates that the instability of the structural properties of the in situ loess caused by the damage is larger at the initial stage. Weak combined water accelerates the degree of damage to the structural skeleton of the soil, thus reducing the load capacity that it can withstand when resisting compression. Under the same external force, the porosity of the model in the weak combined water state is larger than that in the strong combined water state, and the large pores help the particles adjust their angles and positions, resulting in the less obvious form of macroscopic damage and plastic damage.

For the study of structural parameters of loess, previous scholars only stayed in the perspective of water content and compaction [18, 30] and performed mechanical analysis of in situ and remodeled loess and only briefly considered the effect of combined water film, but the mechanical influence mechanism of combined water type was not explored in depth. In this paper, based on the indoor test, combined with the PFC software, the effect of strong and weak combined water on the skeleton structure of in situ loess is studied, to deepen the understanding of the complexity of mechanical properties of in situ loess caused by the difference of water. The study provides theoretical reference for the construction and design of loess subgrade projects.

In the future work, the unsaturated strength characteristics, creep characteristics, and long-term strength index of loess under the influence of combined water can be further tested to deepen the study of the mechanism of the influence of combined water on in situ loess.

6. Conclusions

In this paper, the triaxial test and particle flow numerical simulation test were used to systematically analyze from the macro and meso perspectives, including the influence mechanism of combined water content on the deformation characteristics and mechanical strength characteristics of in situ loess. The main conclusions are as follows.

(1) The failure mode of the sample is greatly affected by the content of combined water. The failure sample under the condition of strong combined water has obvious cracks and shear bands, showing brittle failure. The failure mode of soil samples under weak combined water is characterized by no obvious cracks and overall bulging, showing plastic failure. Weak combined water is the main factor affecting soil deformation

(2) The axial stress decreases with the increase of combined water content, and the stress-strain curve of the specimen in the state of strong combined water is weakly hardened, while the stress-strain curve with weak combined water mainly is strongly hardened. The water content at the boundary of strong and weak combined water is regarded as a distinction between weak and strong strain hardening. As the combined water volume increases, the ultimate strength, structural strength, and structural parameters decrease, leading to a decrease in the structural and deformation resistance of the in situ loess. Strong combined water made the soil have stronger initial stress structure. It shows that the combined water has a greater influence on the structural properties of in situ loess, among which the weak combined water is the most significant

(3) The results of numerical simulation of particle flow show that the directional movement of particles is obvious, the particles at the upper and lower ends are gradually crowded toward the middle and will move along the fracture surface to be destroyed, and this displacement leads to the distribution of cracks or bulging phenomena in the model

(4) The axial compressive stress of the model in the weak combined water state is more pronounced, and the porosity is greater than in the strong combined water stage, accelerating the degree of damage to the structural skeleton of the soil. The large pores help the particles to adjust their angle and position, which makes the interparticle linkage strength lower, the soil strength loss is reduced, and the more pronounced the strain hardening of the model, resulting in a less pronounced and drastic form of macroscopic damage

Data Availability

The data used to support the findings of this study are included within the article.

Conflicts of Interest

The authors declare that there are no conflicts of interest regarding the publication of this paper.

Acknowledgments

The authors express their appreciation for the financial support of the National Natural Science Foundation of China (Grant no. 51878064), Key R & D and transformation plan of Qinghai Province (Grant no. 2021-SF-165), and Natural Science Basic Research Program of Shaanxi (Grant no. 2021JQ-244).

References

[1] G. X. Li, *Advanced Soil Mechanics*, Tsinghua University Press, Beijing, 2004.

[2] R. G. Gu and Y. G. Fang, "Exploration of substance bases and mechanism of soft soil rheology," *Rock and Soil Mechanics*, vol. 30, no. 7, 2009.

[3] C. F. Shen, X. W. Fang, and H. Z. Chen, "Triaxial tests of unsaturated remolded q2 loess," *Chinese Journal of Underground Space and Engineering*, vol. 6, no. 3, pp. 503–508, 2010.

[4] W. Y. Wang, A. M. Li, and X. M. Zhang, "DSC and SEM analysis on bound water characteristics in sewage sludge," *Advanced Materials Research*, vol. 347, pp. 2085–2089, 2011.

[5] D. J. Lee and Y. H. Hsu, "Measurement of bound water in sludges: a comparative study," *Water Environment Research*, vol. 67, no. 3, pp. 310–317, 1995.

[6] S. Li, C. M. Wang, X. W. Zhang, L. Zou, and Z. Dai, "Classification and characterization of bound water in marine mucky silty clay," *Journal of Soils and Sediments*, vol. 19, no. 5, pp. 2509–2519, 2019.

[7] J. T. Liu, Y. K. Fu, T. L. Li et al., "Types of water on the surface of loess and its mineral particles and their quantitative characterization," *Hydrogeology & Engineering Geology*, vol. 49, pp. 105–113, 2022.

[8] Y. Li, T. H. Wang, and L. J. Su, "Determination of bound water content of loess soils by isothermal adsorption and thermogravimetric analysis," *Soil Science*, vol. 180, no. 3, pp. 90–96, 2015.

[9] H. K. Wang, H. Qian, Y. Y. Gao, and Y. Li, "Classification and physical characteristics of bound water in loess and its main clay minerals," *Engineering Geology*, vol. 265, article 105394, 2020.

[10] P. He, Q. Xu, J. L. Liu, C. H. Pu, and D. Chen, "Experimental study on the effect of combined water content on shear strength of remolded loess based on NMR," *Mountain Research*, vol. 38, no. 4, pp. 571–580, 2020.

[11] S. Li, C. M. Wang, Q. Wu, Z. M. Zhang, and Z. N. Zhang, "Variations of bound water and microstructure in consolidation-creep process of Shanghai mucky clay," *Rock and Soil Mechanics*, vol. 38, no. 10, pp. 2809–2816, 2017.

[12] Z. G. Xu, S. X. Feng, J. R. Chai, Y. Tan, and X. Chen, "The effect of initial shear stress of clay bound water on non-Darcy flow," *Journal of Water Resources & Water Engineering*, vol. 28, no. 6, pp. 200–203, 2017.

[13] Q. Yang, "A study on influence of bound water on viscosity coefficient of clays during consolidation," *Science Technology and Engineering*, vol. 17, no. 6, pp. 92–96, 2017.

[14] M. N. Testamanti and R. Rezaee, "Determination of NMR T_2 cut-off for clay bound water in shales: a case study of Carynginia Formation, Perth Basin, Western Australia," *Journal of Petroleum Science and Engineering*, vol. 149, pp. 497–503, 2017.

[15] Q. Wu, X. S. Mao, and C. M. Wang, "Mechanism of bound water effects on the secondary consolidation property of soft soil," *China Journal of Highway and Transport*, vol. 34, no. 7, pp. 215–225, 2021.

[16] S. H. Lei, Z. Y. Li, and J. Q. Wang, "Effect of water content on strength of unsaturated loess," *Journal of traffic and transportation engineering*, vol. 12, no. 1, pp. 21–25, 2012.

[17] J. T. Deng, J. J. Wang, R. E. Li, and X. X. Qiao, "The strength characteristics of undisturbed loess under humidified condition," *Journal of Arid Land Resources and Environment*, vol. 30, no. 1, pp. 136–140, 2016.

[18] B. Wang, R. Huang, X. F. Huang, M. M. Qiu, and H. Wang, "Influence of loess structural parameters on unconfined compressive strength in Yan'an new area," *Journal of Water Resources & Water Engineering*, vol. 33, no. 3, pp. 202–208, 2022.

[19] Y. Z. Hao, T. H. Wang, and J. J. Wang, "Structural properties of unsaturated compacted loess for various sample moisture contents," *Arabian Journal of Geosciences*, vol. 12, no. 8, 2019.

[20] S. B. Li, C. M. Wang, J. Q. Ma, and G. C. Wang, "Microscopic changes of Longxi loess during triaxial shear process," *Rock and Soil Mechanics*, vol. 34, no. 11, pp. 3299–3305, 2013.

[21] M. J. Jiang, T. Li, and H. J. Hu, "Numerical simulation of biaxial tests on structured loess by distinct element method," *Chinese Journal of Geotechnical Engineering*, vol. 35, no. S2, pp. 241–246, 2013.

[22] W. P. Li, S. Z. Yu, and B. R. Wang, "Determination of adsorption and bound water content in deep clayey soil in coal mining area and its significance," *Hydrogeology Engineering Geology*, vol. 3, pp. 31–34, 1995.

[23] X. W. Zhang, C. M. Wang, and J. X. Li, "Experimental study of coupling behaviors of consolidation-creep of soft clay and its mechanism," *Rock and Soil Mechanics*, vol. 32, no. 12, pp. 3584–3590, 2011.

[24] Y. H. Wang, W. K. Ni, and Z. H. Yuan, "Discussion on joint strength theory of intact loess," *Journal of Hefei University of Technology (Natural Science Edition)*, vol. 38, no. 12, pp. 1688–1692, 2015.

[25] H. Zhou and X. S. Mao, "Study on the effect of binding water on the shear strength of loess," *World Forum on Transport Engineering and Technology*, pp. 484–488, 2021.

[26] D. Y. Xie and J. L. Qi, "Soil structure characteristics and new approach in research on its quantitative parameter," *Chinese Journal of Geotechnical Engineering*, vol. 21, no. 6, pp. 651–656, 1999.

[27] C. L. Chen, X. Jiang, T. Z. Su, J. Jing, and W. W. Li, "Influence of soil structure on unconfined compression behaviour of compacted loess," *Chinese Journal of Rock Mechanics and Engineering*, vol. 33, no. 12, p. 22539, 2014.

[28] Z. Wu, S. Xu, D. Chen, D. Zhao, and D. Zhang, "An experimental study of the influence of structural parameters on dynamic characteristics of loess," *Soil Dynamics and Earthquake Engineering*, vol. 132, article 106067, 2020.

[29] J. D. Wang, T. F. Gu, M. S. Zhang, Y. Xu, and J. Kong, "Experimental study of loess disintegration characteristics," *Earth Surface Processes and Landforms*, vol. 44, no. 6, pp. 1317–1329, 2019.

[30] C. Y. Liang, Y. D. Wu, J. Liu, and H. G. Wu, "Influence of soil particle arrangement and cementation on the structure of artificial structural soil," *Chinese Journal of Geotechnical Engineering*, vol. 44, no. 11, pp. 2135–2142, 2022.